Microsc. Microanal. 12, 36–48, 2006
DOI: 10.1017/S1431927606060193

Microscopy AND Microanalysis

© MICROSCOPY SOCIETY OF AMERICA 2006

Tomographic Spectral Imaging with Multivariate Statistical Analysis: Comprehensive 3D Microanalysis

Paul G. Kotula,* Michael R. Keenan, and Joseph R. Michael

Sandia National Laboratories, Materials Characterization Department, P.O. Box 5800, MS0886, Albuquerque, NM 87185-0886, USA

Abstract: A comprehensive three-dimensional (3D) microanalysis procedure using a combined scanning electron microscope (SEM)/focused ion beam (FIB) system equipped with an energy-dispersive X-ray spectrometer (EDS) has been developed. The FIB system was used first to prepare a site-specific region for X-ray microanalysis followed by the acquisition of an electron-beam generated X-ray spectral image. A small section of material was then removed by the FIB, followed by the acquisition of another X-ray spectral image. This serial sectioning procedure was repeated 10–12 times to sample a volume of material. The series of two-spatial-dimension spectral images were then concatenated into a single data set consisting of a series of volume elements or voxels each with an entire X-ray spectrum. This four-dimensional (three real space and one spectral dimension) spectral image was then comprehensively analyzed with Sandia's automated X-ray spectral image analysis software. This technique was applied to a simple Cu-Ag eutectic and a more complicated localized corrosion study where the powerful site-specific comprehensive analysis capability of tomographic spectral imaging (TSI) combined with multivariate statistical analysis is demonstrated.

Key words: tomography, spectral imaging, multivariate statistical analysis, multivariate curve resolution, 3D chemical analysis, tomographic spectral imaging, serial sectioning, 3D microanalysis

Introduction

Chemical analysis is typically performed at points, lines, or over areas in images. This would include single-spectrum acquisitions, line profiles (or spectrum lines), chemical maps (Cosslett & Duncumb, 1956), or spectral images (an image where each pixel contains an entire spectrum) (Legge & Hammond, 1979). Recently, however, interest has been growing in extending microanalysis to the third spatial dimension through three-dimensional (3D) atom probe techniques (see, e.g., references in Miller, 1997) or various direct tomographic (Patkin & Morrison, 1982; Rüdenauer, 1982, 1993; Sharonov et al., 1994; Marschallinger, 1998; Saadi et al., 1998; Dunn & Hull, 1999; Takanashi et al., 2000; Hull et al., 2001; Dunn et al., 2002; Vekemans et al., 2004) or computed tomographic approaches (Schofield & Lefevre, 1992; Schofield, 1995; Möbus & Inkson, 2001; Midgley & Weyland, 2003; Möbus et al., 2003). Each of the techniques referenced above has a combination of useful analytical signal, specimen preparation requirements/limitations, and relevant resolution/total volume sampled as well as various degrees of experimental and computational complexity.

Received February 5, 2005; accepted October 18, 2005.
**Corresponding author*. E-mail: pgkotul@sandia.gov

Table 1 shows some of the direct tomographic methods and their relevant resolutions. With the exception of atom-probe techniques, in which each atom from the specimen is, in principle, identified, and the more recent 3D confocal X-ray fluorescence analysis (Vekemans et al., 2004), only rudimentary acquisition and analysis techniques were applied. For example, elemental maps (spectroscopic images) were acquired from known elements and then rendered in 3D images (Marschallinger, 1998). Spectral imaging approaches (full spectra from each spatial element) have traditionally been limited to smaller numbers of spectra and covering lines or areas. This was due primarily to the lack of the ability to acquire the data in three dimensions or the lack of computational ability to analyze the data (e.g., reconstruct spectra from points/regions, map chemical signals, or perform more sophisticated data analyses). In actuality, methods for the acquisition of extremely large spectral images are commercially available and their comprehensive and unbiased analysis, based on multivariate statistical analysis (MSA), has been developed (Kotula & Keenan, 2003; Kotula et al., 2003*a*) including for 3D spectral images (Kotula et al., 2003*b*, 2004). In contrast, the method described by Vekemans (Vekemans et al., 2004) for the analysis of 3D confocal micro X-ray fluorescence spectral images presumes all of the peak shapes are known *a priori* so that the problem can be reduced from thousands of variables (channels) to 10 or fewer variables (now elements) prior to

Table 1. Comparison of Some Direct Methods for 3D Chemical Analysis

Technique	Lateral/depth resolution (nm)	Total volume sampled	Limitations	References
3D atom probe	0.1/1	10^5 nm^3	Conducting sample	Miller, 1997
LEAP	0.1/1	10^6 nm^3		Kelly et al., 2004
FIB-SIMS	20/20	10 μm^3	Mapping only	Dunn and Hull, 1999
FIB-EDS	100–1000/100–1000[a]	10,000 μm^3	Volume limited by FIB milling time	Kotula et al., 2003*b*, 2004

[a]Dependent on *Z* of material, electron accelerating voltage, and thickness of sections.

multivariate statistical analysis (principal components analysis) and clustering (*k*-means).

In this work, we demonstrate an analytical geometry for tomographic or three-spatial-dimension spectral imaging using a combined focused ion beam (FIB)/scanning electron microscope (SEM)–energy-dispersive X-ray spectrometer (EDS) system with the FIB for serial sectioning and the SEM-EDS for X-ray spectral imaging. We further demonstrate the use of MSA methods for rapid and comprehensive analysis of the very large resultant four-dimensional (4D) data sets. The techniques described herein are more generally applicable to other tomographic methods (e.g., metallography, microtomy, tilt-series reconstructions, etc.) as well other analytical techniques (e.g., time-of-flight secondary-ion mass spectrometry (TOF-SIMS), X-ray photoelectron spectroscopy (XPS), X-ray fluorescence (XRF), particle-induced X-ray emission (PIXE), etc.) where tomographic spectral imaging (TSI) data is or could be acquired, and peak identities, shapes (including families of peaks), positions, and relative intensities may not be known *a priori*.

Materials and Methods

The method used here for sectioning the specimen is similar to that described by Sakamoto et al. (1998) and Dunn and Hull (1999). Serial sectioning was performed with a FEI DB-235, FIB/SEM, equipped with an ultrathin window EDS controlled by a Thermo NORAN Vantage Digital Imaging with Spectral Imaging system. The ion column is cofocal with the field emission SEM and at an angle of 52° with respect to the same. The EDS has a take-off angle of 35° and is at a 45° azimuthal angle with respect to the plane of the ion and electron columns. For the serial sectioning, the sample, initially untilted with respect to the electron beam, is tilted 52° toward the ion column. The ion beam is then normal to the sample surface. It is possible to use other geometries, but the one used facilitated FIB-cut to FIB-cut alignment as will be described below. It is possible then, to cut a cross section with the FIB, image the same surface with the SEM, and detect the resultant X rays with the EDS, all without tilting the specimen.

Prior to FIB cutting, a protective layer of Pt is deposited, over the surface to be cut, with the DB-235's ion-beam-assisted deposition capability. This overlayer serves as a sacrificial layer to prevent milling/Ga implantation of the surface so the original sample surface is preserved, and this overlayer can be used as a fiducial alignment reference. Additionally, two fiducial markers are milled into the surface with the FIB: one parallel to the analysis surface set back several microns beyond anticipated milling and one perpendicular to the first that acts as a lateral alignment reference. In later experiments, a pattern was milled into the sample surface with spacings of 0.5 μm perpendicular to the milling direction. This made measurements of the amount of material removed for each slice unnecessary. To image the initial analysis surface with electrons, however, a FIB stair-step cut is made, shallow away from the analysis surface and deeper near to it. Additionally, another FIB stair-step cut is cut at right angles with respect to the first, on the side of the analysis surface toward the EDS. This ensures that there is no shadowing of the analysis surface with respect to the EDS by any intervening specimen. The analytical geometry as seen from the point of view of the EDS is shown in the secondary-electron image of the analysis surface in Figure 1a and schematically in Figure 1b.

A 50-μm-wide analysis surface was milled of which ~33 μm were analyzed via X-ray spectral imaging. Approximately 1 μm of material was removed from the sample for each slice, exposing a new analysis surface, with a 5-nA ion beam of approximately 50 nm diameter. The specific amount of material removed was measured with an ion-beam image of the specimen surface, making reference to the fiducial markers. Electron-beam image shifting, using the fiducial mark perpendicular to the analysis surface as well the original specimen's surface, was used to realign the analysis region for successive X-ray spectral image acquisitions. For the initial trenching, a relatively large high-current ion beam was used, whereas finer cuts, made prior to the first and subsequent spectral image acquisitions, are made with a much smaller and therefore lower-current ion beam, resulting in a smoother analysis surface. It should be noted here that the ion imaging step, for fiducial marker measurement,

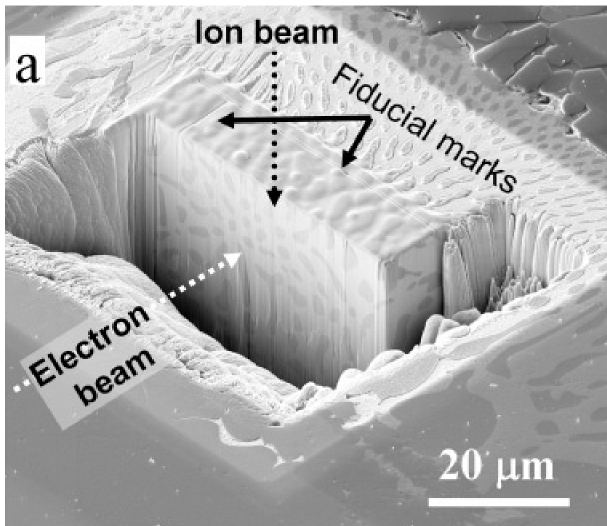

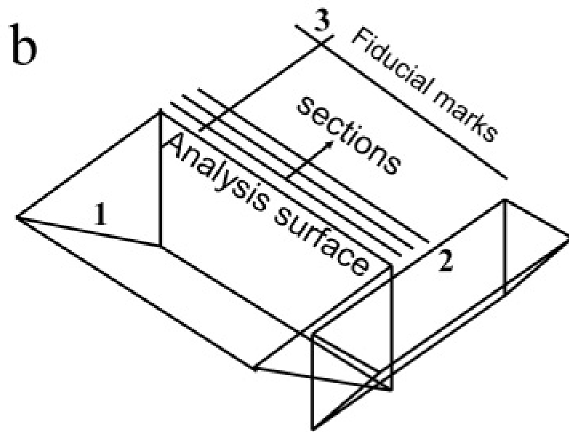

Figure 1. **a**: Secondary-electron image taken to approximate the view of analysis surface seen by the X-ray spectrometer. **b**: Schematic of the analysis geometry with (1) first stair-step trench, (2) second stair-step trench, and (3) fiducial markers.

results in a small amount of sputtered material on the analysis surface. This was experimentally found to eliminate charging during electron imaging of nonconducting surfaces.

X-ray spectral images, 128 by 128 pixels by 512 or 1024 channels were acquired from each slice at electron-beam excitations of 5 and 10 kV, respectively. For spectral image acquisition, the electron column was operated at 3000× magnification, resulting in a lateral field of view in the spectral images of 40 μm (300 nm/pixel) and a vertical field of view of 51 μm (400 nm/pixel). The vertical field of view is larger than the lateral field of view due to the specimen tilt of 52° of the electron beam with respect to the plane of the analysis surface. Of that available vertical field of view, however, only about 28 μm were utilized, as the rest were either foreground or background, out of the plane of analysis. The reduction was made off-line, after the data were acquired and analyzed, by truncating groups of voxels away from the analysis surface. For the first cuts, the stair-step

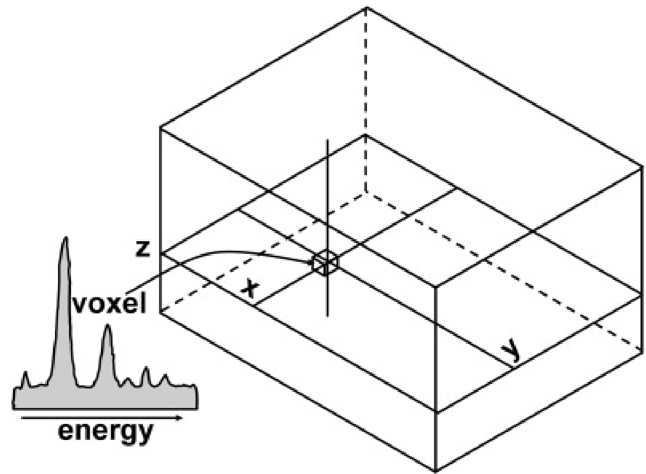

Figure 2. Schematic of the four-dimensional tomographic spectral image data set. Each voxel or volume element has three spatial coordinates and one energy dimension.

trench was shallower than for subsequent cuts, so that more of the analysis surface was visible to the electron beam as the acquisition went on. This resulted in a tapering of the volume sampled by this technique. For the two examples presented in this article, 10–12 slices were made with approximately 1 μm being removed per slice. Given the excitation volumes expected, in the materials analyzed, the information in the z direction was most likely undersampled whereas that in the x and y directions was for the most part oversampled. These dimensions could be increased at the expense of the additional time needed to mill the analysis surface.

The TSI resulting from the above procedure was then analyzed using the approach previously described (Keenan & Kotula, 2003, 2004*b*; Kotula et al., 2003*a*) but will be briefly described here. The tomographic spectral image is shown schematically in Figure 2 as a series of spectra, each from a voxel sampling a volume of material. The goal of the MSA is to factor this raw spectral image, which can consist of tens of thousands to millions of spectra, into a more compact and readily interpreted form. The equation being solved is

$$\mathbf{D} = \mathbf{C}\mathbf{S}^T \tag{1}$$

where **D** is the raw X-ray spectral image data matrix unfolded as m voxels by n channels, **C** is a matrix of abundances of the components (m voxels by p components) or the component images (suitably refolded), **S** is a matrix of component spectral shapes (n channels by p components), and the superscript T denotes the matrix transpose. The determination of the number of components, p, to retain for the linear model will be described below. The process of generating spectral images from the serial sections and unfolding the data from all the slices into the matrix **D** is

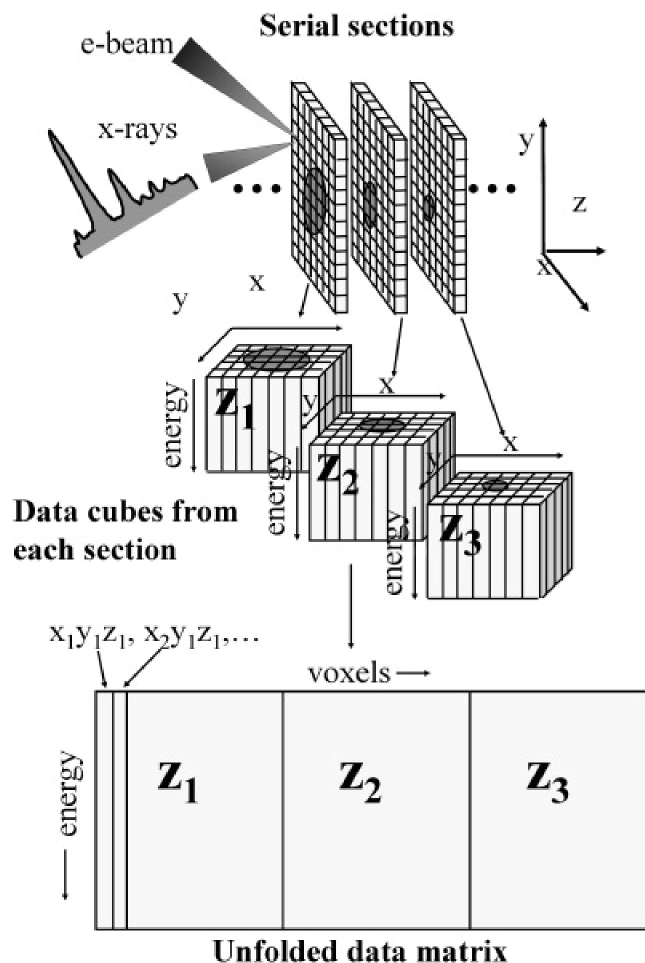

Figure 3. Schematic of the procedure for generating the tomographic spectral image data set and unfolding it into a matrix for the subsequent multivariate statistical analysis calculations.

shown schematically in Figure 3. There is no fundamental difference, as far as the algorithms are concerned, with respect to the dimensionality of the data. The data could be a series of point analyses from different specimens and therefore have no point-to-point spatial correlation. The data could also be a one-dimensional spectral line, two-dimensional spectral image (2D), 3D tomographic spectral image, time resolved series of spectra, and so forth, and the underlying data analysis algorithms are no different. The only difference is how the output matrix **C** is displayed.

The first step in the MSA calculation is to normalize the raw data for Poisson statistics (Keenan & Kotula, 2004*a*). If this is not done, large variations in the raw data, due to noise, are fit by the algorithms at the expense of smaller, but chemically significant, spectral features. That is, in the absence of Poisson weighting, it is more profitable in a least-squares sense to fit large magnitude differences due to noise in high-intensity channels rather than smaller but chemically significant signals. Next, an eigenanalysis is performed on the weighted data to determine the number of significant factors p to retain in the calculation. A semi-log plot of the sorted eigenvalues consists of a baseline of eigenvalues (straight line on the semi-log plot) that describes noise and typically, several eigenvalues that rise above the noise baseline, thus describing non-noise signals in the data. These non-noise signals are typically chemical in nature but may also describe artifacts in the data. The number of non-noise eigenvalues is p, the number of linearly independent components that will be used to model the raw data in the model described in equation (1). The choice of the correct number of components to retain, p, is automatically made by fitting a straight line to a range of the eigenvalues that describes noise. If an eigenvalue sits above the extrapolation of this line by a sufficient amount, it is deemed significant, and that value sets the cutoff point below which all components describe noise. The solution will then be the most compact possible given the rank-one approximation to the noise (Keenan & Kotula, 2004*a*), describing the most chemical information in the fewest chemical components, in a computationally inexpensive and routine way.

After weighting the data and determining the correct number of components or factors to retain in the model, the next step is multivariate curve resolution implemented via an alternating least squares approach (MCR-ALS) (Tauler & de Juan, 2002; Keenan & Kotula, 2003, 2004*b*). MCR-ALS is a constrained factor analysis approach where equation (1) is solved in an iterative fashion. After making an initial estimate of either C or S, conditional estimates of C and S are obtained, alternately, given the preceding estimates of the complementary factors. This process continues until a convergence criterion is met. All estimates are made using least squares procedures and are subject to physically appropriate constraints. In the present case, an initial guess for S is derived from the eigenvectors above, and the spectral shapes S and concentrations C are constrained to be non-negative. Following the application of MCR-ALS the resultant C and S matrices are inversely scaled back into the space of real spectra and abundances. The result is a parsimonious representation of the data that uses the smallest possible number of chemical components needed to completely describe the chemical information in the data in a physically realistic and readily interpretable way. The calculations were performed with an optimized C++ code implemented on Windows™-based personal computers with Intel™ processors (Keenan & Kotula, 2003, 2004*b*).

The data sets from the Cu-Ag eutectic and localized corrosion specimens consisted of 10 slices each with 128 by 128 pixels by 1024 and 512 energy channels, or approximately 168 million (671 Mbytes) and 84 million (335 Mbytes) data elements, respectively. On a dual 2.4-GHz Pentium IV Xeon computer equipped with 2 Gbytes of RAM, the analysis of the localized corrosion TSI took 51 s and required only 435 Mbytes maximum of system memory. On a somewhat limited laptop (Single 1.1 GHz Pentium III, with 512 Mbytes RAM), the same analysis took 192 s and would have

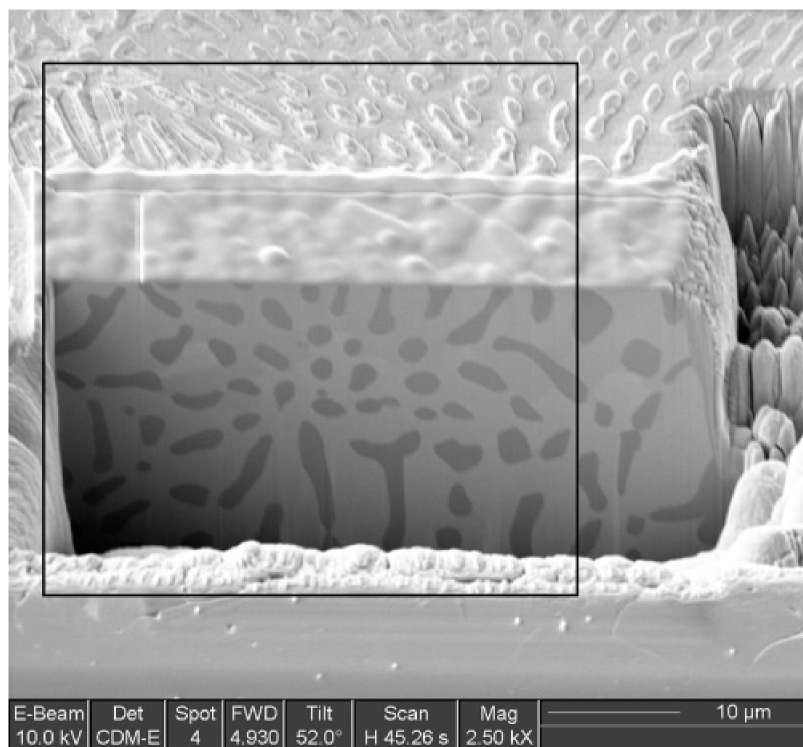

Figure 4. Secondary electron image of slice 12, from the perspective of the electron column. The box indicates the position of the spectral image acquisition.

exceeded the free system memory if the calculation had not been performed with out-of-core memory algorithms (Kotula & Keenan, 2003). For comparison, the total number of data elements (*x*, *y*, *z*, element) analyzed in Vekemans' work (Vekemans et al., 2004) was fewer than 300,000 (in an unspecified time) compared with 80–160 million in the present work with computational times less than 1 min. For rendering, the component images were converted from the matrix of concentrations, *C*, to a series of tif images corresponding to the planes of the original slices with a Matlab™ script. The 3D component images were all rendered with the commercial software package Imaris™. Imaris performed both linear interpolation and smoothing on selected component images. When smoothing was applied, a Gaussian filter with a width of approximately 1.5 × the voxel × dimension was used, which corresponded to approximately 400 nm. The Cu-Ag eutectic example was not Gaussian smoothed, whereas all but the Ni component image in the corrosion example was Gaussian smoothed. Snapshots of different orientations are shown in the figures with links in the figure captions, in selected cases, to full animations.

Results

Cu-Ag Braze Joint

The first example of a TSI analyzed with the MSA procedure described above was from a Cu-Ag braze joint between Kovar (an Fe-Co-Ni alloy) and alumina. Data were only acquired nominally from the Cu-Ag eutectic alloy region, making this a chemically simple example with two expected chemical phases. Although this example could have been analyzed via electron images of the serial sections alone, it represents a proof of concept of the TSI acquisition and MCR techniques. The specimen was prepared as a metallographic cross section of the braze joint with the FIB being used to cut sections perpendicular to the surface of the metallographic section, parallel to the braze interfaces and adjacent to the Kovar. Figure 4 is a secondary electron image of the last section of the Cu-Ag eutectic (Cu is dark and Ag is light) as seen from the perspective of the electron column during spectral image acquisition. The resultant component images and spectral shapes from the MCR analysis of the data for this one slice are shown in Figure 5. The Pt component results from the Pt deposited in the FIB on the specimen prior to sectioning to protect the top surface from sputtering, Ga implantation, and also so that the surface can be used as a fiducial marker for alignment of the specimen during TSI acquisition. It is clear from Figure 4 that significant topography has developed on the unprotected specimen's surface as seen by the relief in the Ag in the background. The Ga component shown in Figure 5e results from both implantation of Ga and resputter of Ga, Cu, and Ag. This is particularly evident on the sidewall of the trench in front of the analysis surface. As this is the last section from the specimen, significant material has deposited on the sidewall so that it becomes visible in

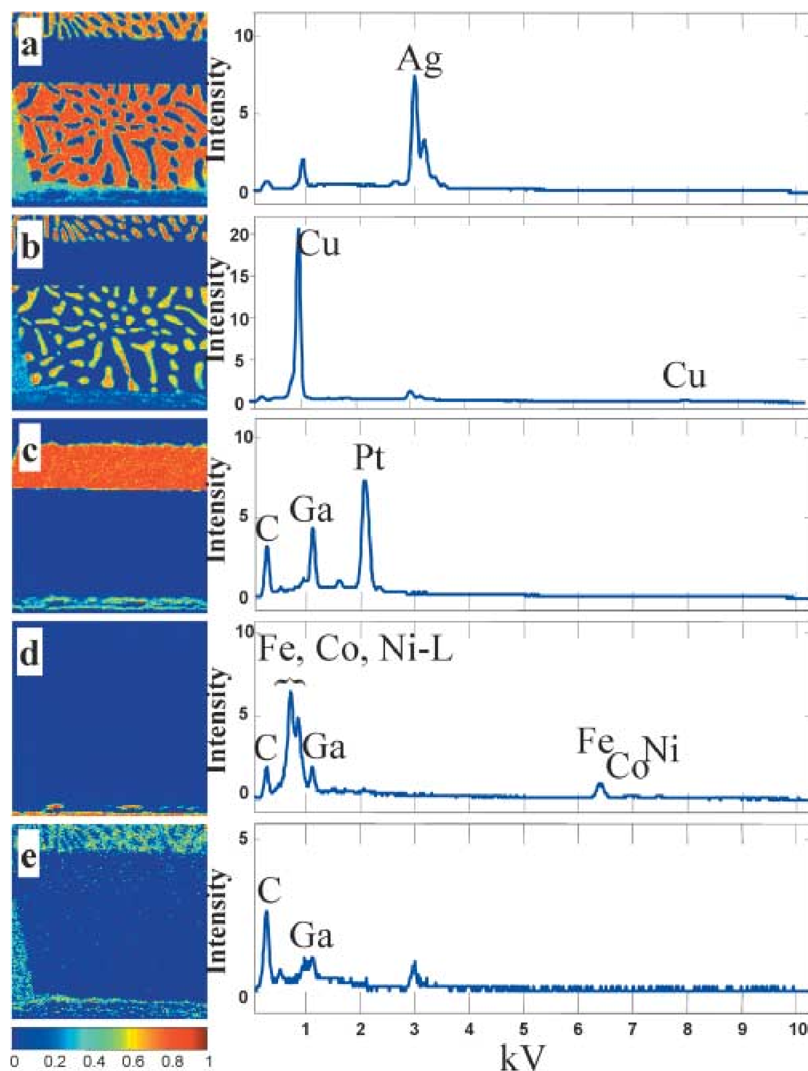

Figure 5. Results of the automated X-ray spectral image analysis of the region of slice 12 shown in Figure 4. Respective component images (left) and corresponding spectral shapes (right) for silver (**a**), copper (**b**), platinum (**c**), Kovar (**d**), and carbon and gallium (**e**). The component images are shown with a spectral color scale with dark blue being zero abundance and dark red being maximum abundance.

the analysis region. In subsequent work, a wider analysis surface trench was cut and was periodically remilled to prevent this buildup from becoming visible during TSI acquisition. The Fe-Co-Ni component shown in Figure 5e results from the adjacent Kovar in the foreground. Although there is significant spectral overlap of the Ga-, Cu-, Fe-, Co-, and Ni-L X-ray lines, as seen in Figure 5, the analysis easily separates the overlaps of the spatially distinct chemical components. For the purposes of the analysis at hand, the components from off of the analysis surface (i.e., Pt, Kovar, and C-Ga) can be disregarded. Additionally, the Cu and Ag component images can be truncated to remove the background regions of Cu and Ag. Results from the analysis of the full (i.e., multislice) TSI shown below reflect this (postacquisition and post-MSA data analysis) editing.

The MCR analysis of the full TSI from the eutectic example resulted in a similar set of component spectral shapes as shown in Figure 5 for the single slice. The component images are now, however, three-dimensional. Several different viewpoints of both the Cu and Ag are shown with a link[a] in the figure caption to animations of both in Figure 6. Additionally, the connectivity of the Cu lamellae is evident in Figure 7, where the regions that are connected are shown in the same color. These connected regions either grew from the same source or impinged (actually or apparently due to the resolution of the measurement) upon an adjacent region. In an effort to more realistically render the 3D component images on a 2D medium, red–cyan anaglyphs were rendered of the components in Figure 8 for two different perspectives. Red (left-eye) and cyan or blue (right-eye) glasses are required to effectively view the anaglyphs. The component images were rendered in gray scale and the stereo feature within Imaris was used to create the ana-

[a]Animations listed in the captions of the Figures 6, 8, and 11 can be accessed at the *Microscopy and Microanalysis* website: http://www.journals.cambridge.org/jid_MAM.

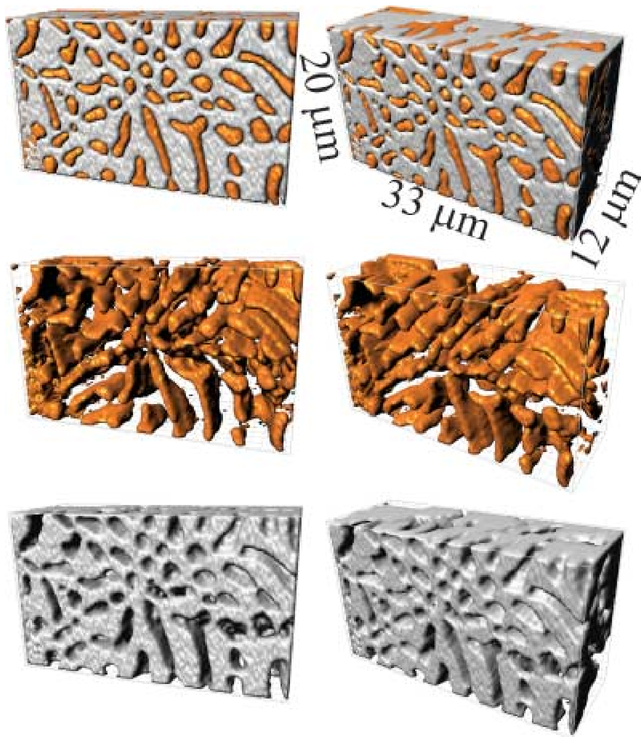

Figure 6. Eutectic example, simultaneous views of Cu and Ag (top), Cu (middle), and Ag (bottom) component images. Click on the following links to see the animation: Kotula_Figure6_Ag.avi, Kotula_Figure6_Cu.avi.

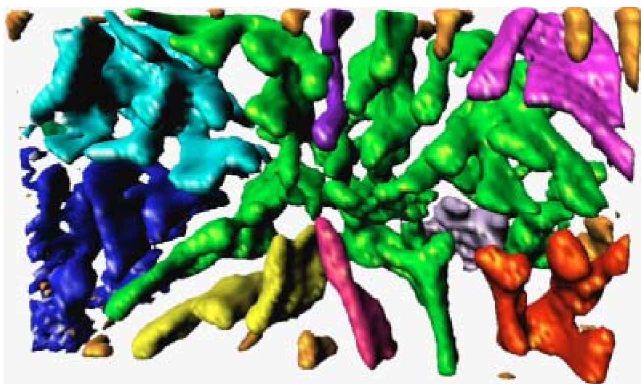

Figure 7. Cu component image color-coded by connectivity. Cu lamellae of similar color are connected with the exception of the small orange regions near the edges of the volume.

glyphs. Additionally, there is a link to several animations of the anaglyphs in the figure caption.

Although the contrast alone in, for example, a series of backscattered electron images, would probably be enough for the reconstruction at hand, the chemistry revealed by the TSI/MSA approach has even greater contrast (albeit at lower spatial resolution) and is furthermore unbiased. In more chemically complex analyses, conventional image con-

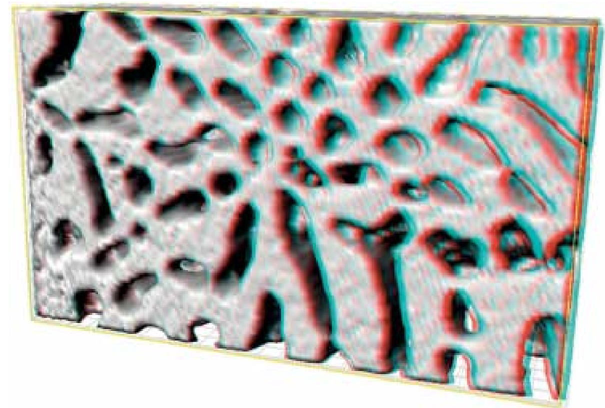

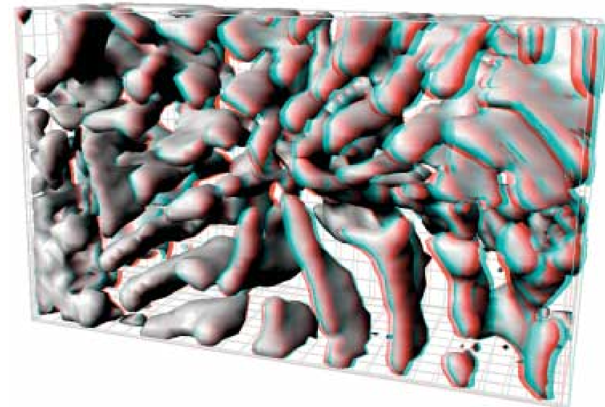

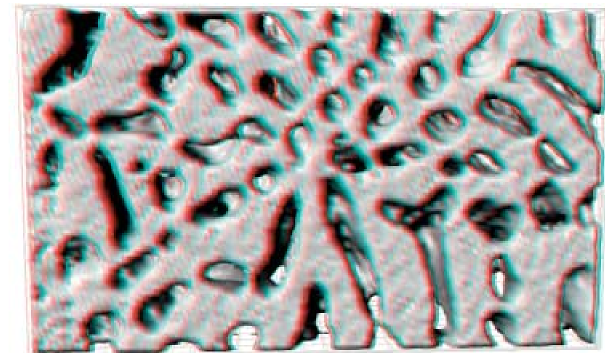

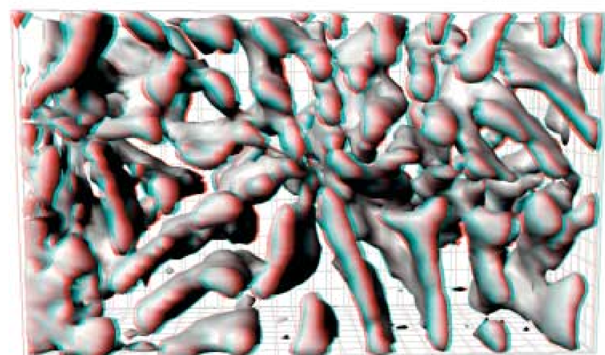

Figure 8. Red/cyan anaglyphs of both the Ag (top) and Cu (bottom) component images. Click on the following links to see the animation: Kotula_Figure8_Ag_anaglyph.avi, Kotula_Figure8_Cu_anaglyph.avi.

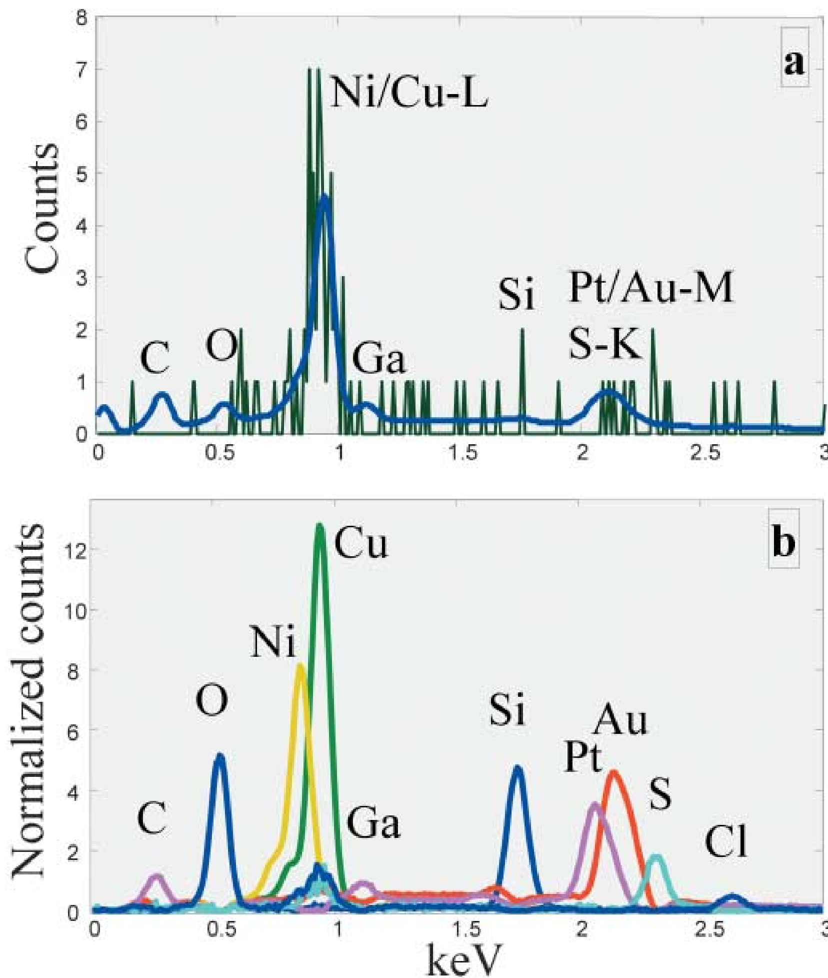

Figure 9. a:. Mean spectrum from the corrosion TSI (blue) and raw spectrum from one pixel of Cu (green). **b**: Spectral shapes from the automated analysis of the TSI. Note the significant spectral overlap between Ni/Cu and Pt/Au/S.

trast alone is insufficient to discriminate all of the possible elemental combinations that might give equivalent contrast. The same could be said of simple 3D chemical mapping with X rays (Marschallinger, 1998) where pathological overlaps of X-ray lines or other potential artifacts could lead to erroneous interpretation of the contrast. Therefore, truly comprehensive chemical analysis is essential—full tomographic spectral images analyzed in their entirety with no preconceptions of the presence or absence of microchemical features. The above example illustrates the chemical specificity of the combined TSI/MSA approach for comprehensive 3D microanalysis in a chemically simple system. Its potential for more chemically complex analyses will be made clear below.

Corrosion of Cu Substrate

In a more chemically complex 3D analysis problem, the cause of a localized corrosion problem was examined. Ni and Au were electroplated on a Cu substrate and exposed to a standard accelerated industrial indoor corrosive environment consisting of H_2S, NO_2, Cl_2(g), and H_2O (70% humidity), at 30°C. Micron-sized protuberances, expected to be a corrosion product, were observed to form on the surface at widely separated locations. EDS analysis confirmed that the outgrowths contained Cu and S. The cause of the localized corrosion was expected to be pinholes in the Ni and/or Au films, but the actual cause was unknown. Because the localized corrosion product was readily visible in the FIB/SEM with the SEM, one outgrowth was located and a 50-μm^2 region including it was coated with electron-beam-assisted Pt followed by ion-beam-assisted Pt to protect the top surface from implantation and sputtering by the Ga ion beam. The TSI had, on average, 140 counts per voxel and contained 23 million counts total. The Pt overlayer also serves to delineate both the top surface of the surrounding region as well as the corrosion product itself. As with the previous example, for rendering of the 3D component images, the regions away from the analysis surface were truncated.

Figure 9a shows both the mean spectrum and a typical raw spectrum from one voxel of Cu, and Figure 9b shows the component spectral shapes, **S**, from the automated analysis of the TSI. Because the data were generated with an incident electron-beam energy of 5 keV, all of the expected elements in the analysis volume (Cu, Ni, Pt, Au, S) have X-ray lines of reasonable intensity. Additionally, most other

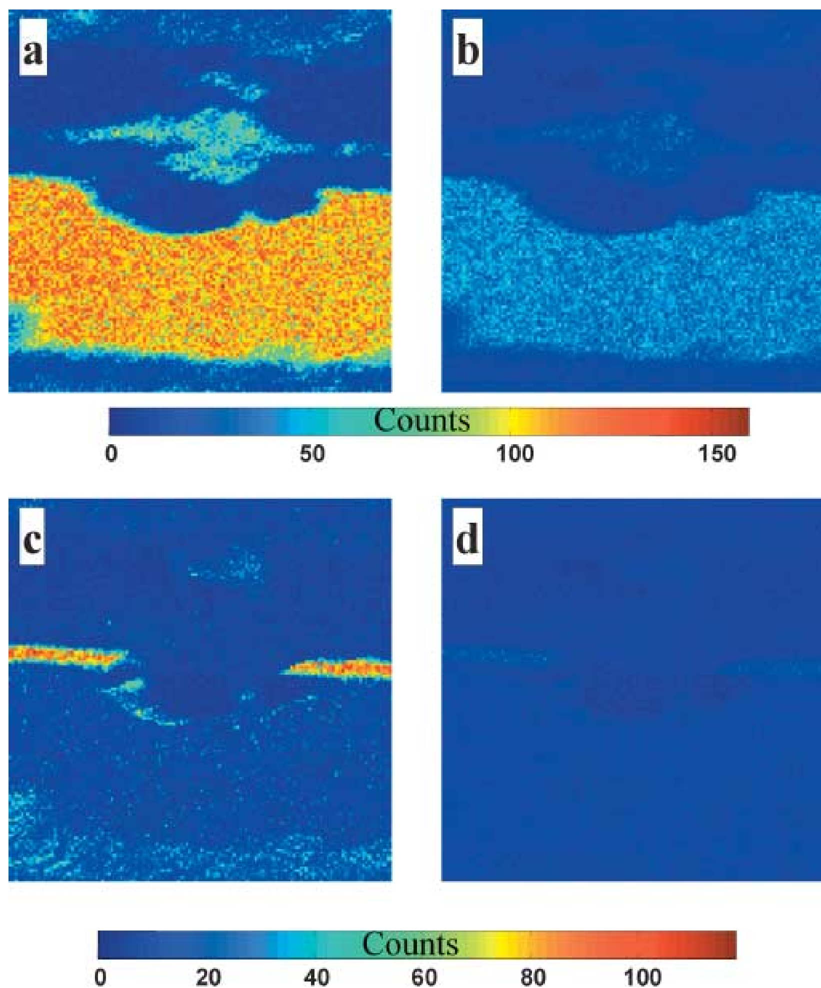

Figure 10. Comparison of respective component images and optimized maps for Cu and Ni on the same intensity scales for slice number 5. **a**: Cu component image. **b**: Cu map from 950 eV to 1030 eV. **c**: Ni component image. **d**: Ni map from 750 eV to 830 eV.

elements, with the exception of H through Be, also have detectable X-ray lines that fall within this excitation limit, although some possible ones might be expected to be difficult to distinguish (e.g., Cr-L and O-K). However, significant spectral overlap is expected for spatially adjacent Ni/Cu, Pt/Au, and Au/S, rendering conventional X-ray mapping less than optimal for displaying the elemental distributions. The advantages of MCR over conventional mapping is quite clear from Figure 9, where Cu- and Ni-L as well as Pt-, Au-M, and S-K X-ray lines, have successfully been deconvolved in spite of significant spectral overlap. Additionally, the respective 3D component images demonstrate this deconvolution capability, resulting in high contrast, as will be shown below. Although 5 chemical components were expected, based on prior knowledge (Cu, Ni, Au, Cu-S, and Pt-Ga-C), the automated analysis found 10. One of the extra components corresponded to a Si-O region and another corresponded to a region that contained Ni, Cu, O, and Cl. The remaining three components from the analysis, which were not rendered, included a noise component (large noise peak) that was not spatially correlated with the microstructure, a carbon component from contamination away from the analysis surface, and a second Pt-Ga-C component representing the e-beam-deposited Pt from the FIB, differing only by the relative amounts of Ga and Pt.

As a direct comparison between conventional maps extracted from the raw spectral image and the MCR approach, Figure 10 shows the pure components from the MSA analysis as well as the optimized X-ray maps for Cu and Ni for one section. The energy ranges for the maps were chosen to minimize the known spectral overlap and the component images were normalized so that the corresponding spectral shapes had an intensity of one count. Therefore the intensities in the component images represent the total number of counts from the respective material-characteristic peaks as well as bremsstrahlung spectral background. It is clear that significant signal has been discarded by simply mapping a small region of spectral intensity.

The component images from MSA, which show the spatial distribution of the respective spectral shapes, are rendered in Figure 11. With this high-contrast direct tomographic analysis, the various chemical components can be visualized individually or together. For example, the starting surface prior to electrodeposition must have looked very

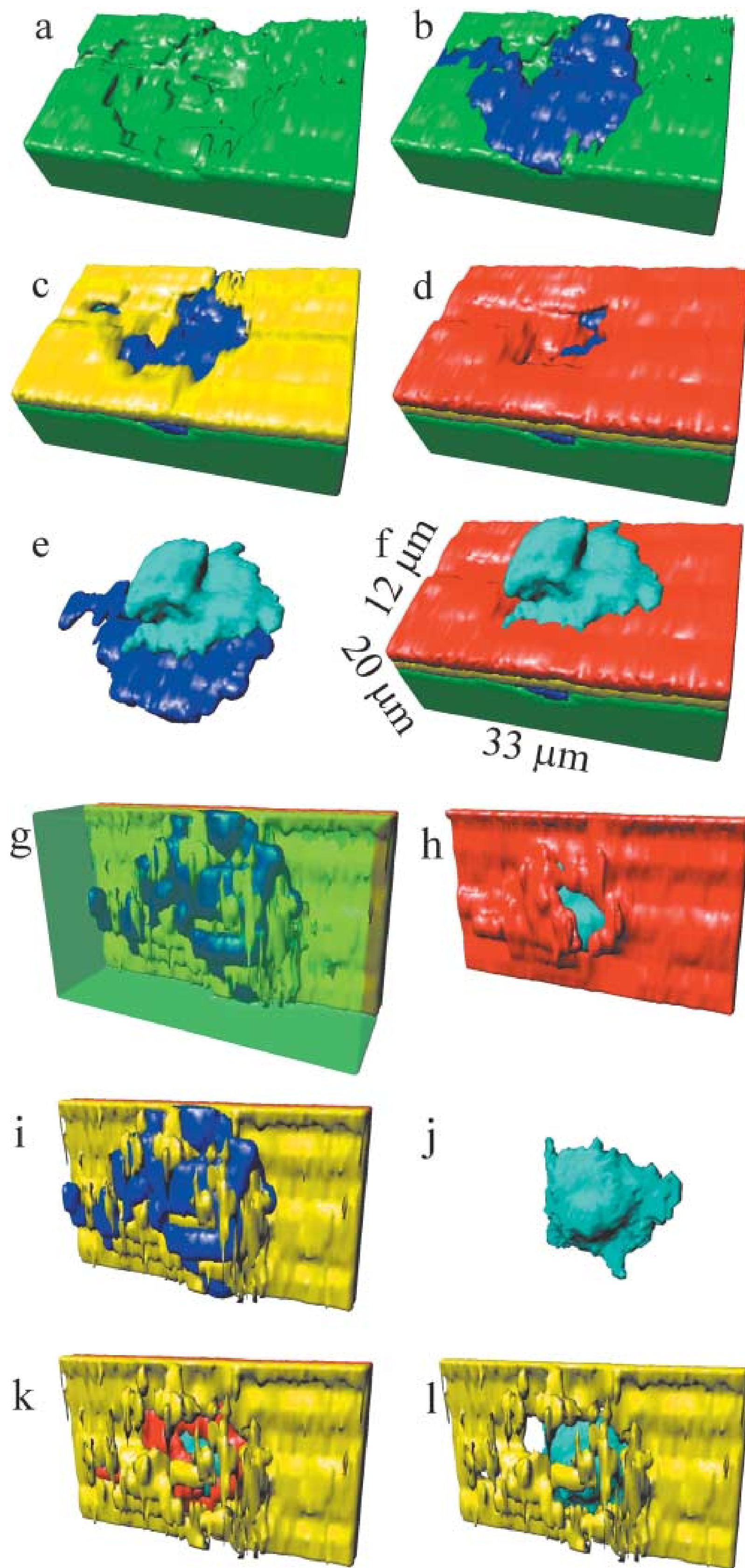

Figure 11. Selected view of the 3D component images from the corrosion example. Red is gold, green is Cu, blue is Si-O, cyan is Cu-S, magenta is Pt, yellow is Ni. Click on the following link to see the animation: Kotula_Figure11_ corrosion.avi.

much like the rendering in Figure 11b, which shows the Cu and Si-O component images rendered together. In contrast the Cu surface can be examined by itself as in Figure 11a. In sequence, the order of development of the microstructure can be followed. Figure 11a is the Cu surface, which had been intentionally roughened by grit blasting with silica particles. The surface as seen by the plating bath consists mostly of Cu but with some Si-O apparently embedded as seen in Figure 11b. This has important consequences for the electroplating process because nonconducting contaminants on the surface will only be plated slowly by deposition starting at the edges. Figure 11c, which shows Cu, Si-O, and Ni, illustrates this. The Ni has only partially overplated the Si-O particle. The gold layer nearly covers the hole in the Ni film, as seen in Figure 11d, but there is still a hole of several square microns in area. This hole allows the environment to reach the less noble metals below and therefore the corrosion process has a pathway to proceed. The spatial association of the unexpected surface contaminant and the resulting corrosion product is shown in Figure 11e. The center of the hole in the gold film directly corresponds to the location of both the Si-O contaminant and the corrosion and all of the respective chemistry can be visualized from various renderings of the 3D component images from the MSA of the TSI. All of the components except the Pt-Ga-C are shown in Figure 11f, along with the dimensions of the rendered volume.

To better see the various layers and plating defect, Figure 11g–l shows the underside of the corroded region. Figure 11g shows the underside of the Ni layer through a translucent-rendered Cu. Figure 11h shows the underside of the gold film and the pinhole that allowed corrosion to proceed and Figure 11i–l shows other combinations of the various materials from the underside. A link to an animation of all the components can be found in the figure caption.

For additional aid in visualizing the three-dimensional component images, they were rendered as red–cyan anaglyphs in stacked sequence in Figure 12. The interlocking nature of the different materials is particularly evident. This method of visualization also allows the topology of the different surfaces to be made clear.

Discussion

The specific details of the tomographic methods described in this article, namely the acquisition of electron-excited X-rays from surfaces revealed by the FIB, should not overshadow the very general applicability of this TSI acquisition and data analysis approach. Other direct TSI acquisition methods would include removing layers of material from a specimen via metallography (Marschallinger, 1998) or microtomy (Denk & Horstmann, 2004) followed by some sort of spectral imaging of the exposed surface with the TSI resulting from multiple iterations of sectioning and spectral imaging. An example of this approach, which demonstrates the power of the method and also the potential for generating extremely large resultant TSI data sets, is metallographic sectioning, which results in a large flat surface for analysis. With current commercially available X-ray spectral image acquisition hardware, spectral images with 1024×1024 pixels (over 1 million spectra) each with 1024 or more channels can easily be acquired. These data sets are 4 Gbytes uncompressed and have already been analyzed with the MSA techniques described above (Kotula & Keenan, 2002). If the TSI had data from 10 sections it would be over 40 Gbytes, and at 50 sections the data set would be in excess of 200 Gbytes. To collect such data sets in a reasonable time (less than 8 h including sectioning time) with current X-ray detectors (e.g., Si-Li) they are by necessity very noisy. It should be noted however that newer commercially available Si-drift detectors could improve this situation by an order of magnitude of more. In previous work, large spectral images with as few as five counts per 1024-channel spectrum have been successfully analyzed with the same algorithms as above, augmented by spectral and spatial compression (Kotula & Keenan, 2003). The ability to analyze extremely noisy data would be useful, as the acquisition times for such data sets could quickly become a limiting factor. The MSA approach described here does make full use of all the statistics and furthermore has been shown to work on more than just X-ray spectral image data: TOF-SIMS (Ohlhausen et al., 2004; Smentkowski et al., 2004) and EELS (Keenan & Kotula, 2004*c*). Therefore one could envision using a microtomy technique to reveal layers of a biological material followed by surface or thin-section analysis to extract not only elemental phase distributions but also molecular signatures. Additionally, the data analysis methods described here could be used to analyze spectral image data acquired from tilt series.

Conclusions

The power of the MSA approach described here is in its robust and unbiased depiction of the large amount of chemical information contained in spectral series and tomographic spectral images. In the examples above, each data element (channel) from each spectrum from over 160,000 voxels has been analyzed, resulting in a small number of chemically relevant component spectra and respective images. The chemical contrast has been maximized and is unambiguous, making this approach superior to conventional rendering approaches such as simple X-ray mapping. The combination of three-spatial-dimensional spectral imaging with comprehensive and unbiased multivariate statistical analysis is a powerful new approach for materials characterization.

The data in the present case were acquired manually. Spectral images from each slice were acquired followed by manual cutting and alignment steps. This entire process could be fully automated, resulting in the ability to cut larger areas with greater efficiency and reproducibility.

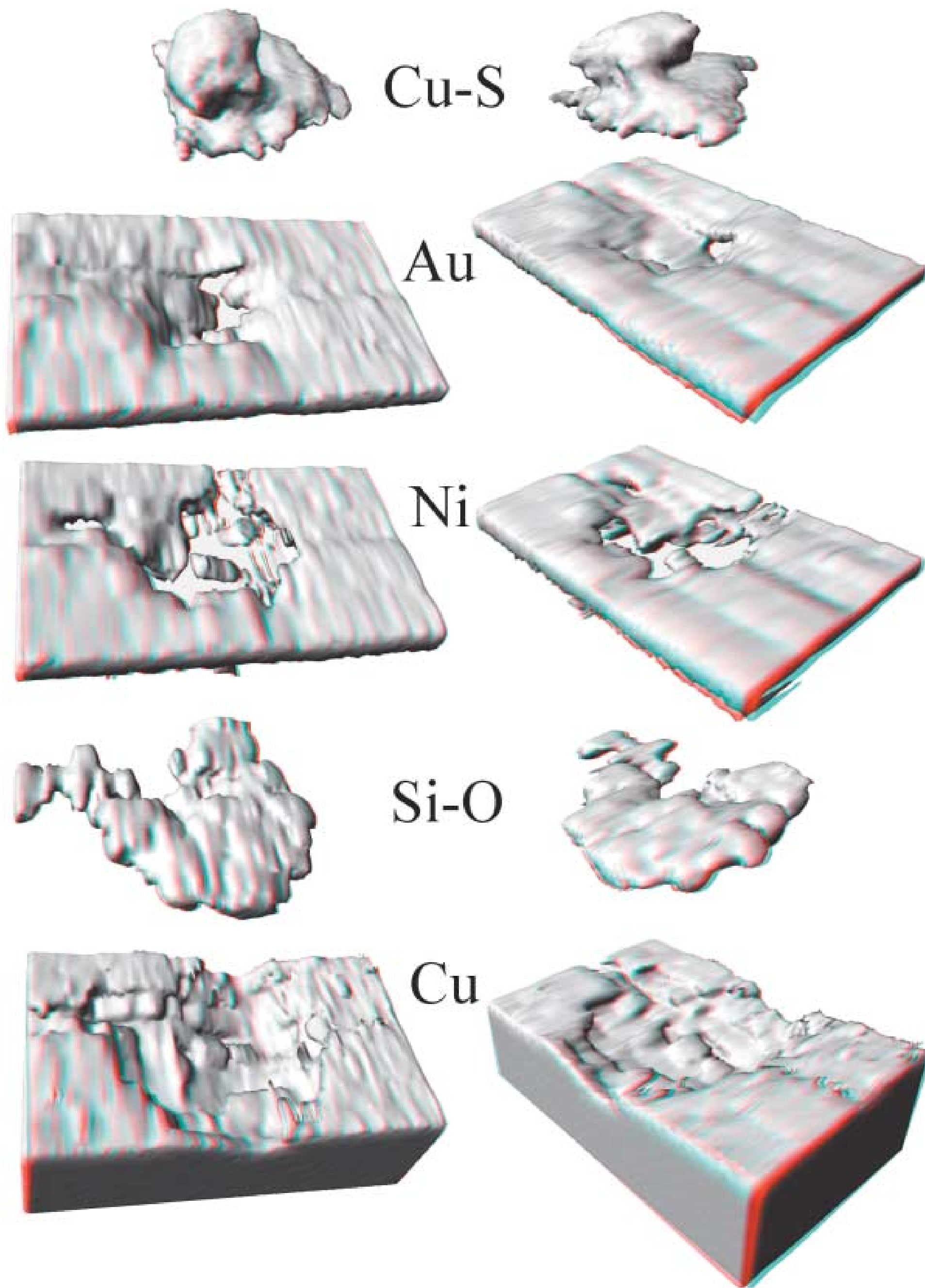

Figure 12. Red/cyan anaglyphs of two views of the 3D component images from the corrosion example.

Acknowledgments

The authors would like to acknowledge Rob Sorensen for provision of the localized corrosion specimen, Luke Brewer for carefully reviewing the manuscript, and Michael Rye for assistance in acquiring some of the TSI data and for developing improved fiducial markers. Sandia is a multiprogram laboratory operated by Sandia Corporation, a Lockheed Martin Company, for the United Stated Department of Energy (DOE) under contract DE-AC04-94AL85000.

References

Cosslett, V.E. & Duncumb, P.D. (1956). Micro-analysis by flying-spot X-ray method. *Nature* **177**, 1172–1173.

Denk, W. & Horstmann, H. (2004). Serial block-face scanning electron microscopy to reconstruct three-dimensional tissue nanostructure. *PloS Biol* **2** [11] (e329), 1900–1909.

Dunn, D.N. & Hull, R. (1999). Reconstruction of three-dimensional chemistry and geometry using focused ion beam microscopy. *Appl Phys Lett* **75**, 3414–3416.

Dunn, D.N., Shiflet, G.J. & Hull, R. (2002). Quantitative three-dimensional reconstruction of geometrically complex structures with nanoscale resolution. *Rev Sci Instrum* **73**, 330–334.

Hull, R., Dunn, D. & Kubis, A. (2001). Nanoscale tomographic imaging using focused ion beam sputtering, secondary electron imaging and secondary ion mass spectrometry. *Microsc Microanal* **7** (Suppl. 2) 934–935.

Keenan, M.R. & Kotula, P.G. (2003). Apparatus and System for Multivariate Spectral Analysis, US Patent # 6,584,413.

Keenan, M.R. & Kotula, P.G. (2004*a*). Accounting noise in the multivariate statistical analysis of TOF-SIMS data. *Surf Int Anal* **36**, 203–212.

Keenan, M.R. & Kotula, P.G. (2004*b*). Method of Multivariate Spectral Analysis. US Patent # 6,675,106.

Keenan, M.R. & Kotula, P.G. (2004*c*). Multivariate statistical analysis of EEL-spectral images. *Microsc Microanal* **10** (Suppl. 2 Proceedings), 874–875.

Kelly, T.F., Gribb, T.T., Olson, J.D., Martens, R.L., Shepard, J.D., Wiener, S.A., Kunicki, T.C., Ulfig, R.M., Lenz, D.R., Strennen, E.M., Oltman, E., Bunton, J.H. & Strait, D.R. (2004). First Data from a Commerical Local Electrode Atom Probe (LEAP). *Microsc Microanal* **10**, 373–383.

Kotula, P.G. & Keenan, M.R. (2002). Spectral imaging: Towards quantitative X-ray microanalysis. *Microsc Microanal* **8** (Suppl. 2 Proceedings), 440–441.

Kotula, P.G. & Keenan, M.R. (2003). Automated analysis of large (>4 Gb) spectral images with efficient out-of-core RAM algorithms. *Microsc Microanal* **9** (Suppl. 2), 152–153.

Kotula, P.G., Keenan, M.R. & Michael, J.R. (2003*a*). Automated analysis of EDS spectral images in the SEM: A powerful new microanalysis technique. *Microsc Microanal* **9**, 1–17.

Kotula, P.G., Keenan, M.R. & Michael, J.R. (2003*b*). Tomographic spectral imaging: Microanalysis in 3D. *Microsc Microanal* **9** (Suppl. 2), 1004–1005.

Kotula, P.G., Keenan, M.R. & Michael, J.R. (2004). Tomographic spectral imaging with a dual-beam FIB/SEM: 3D microanalysis. *Microsc Microanal* **10** (Suppl. 2), 1132–1133.

Legge, G.J.F. & Hammond, I. (1979). Total quantitative recording of elemental maps and spectra with a scanning microprobe. *J Microsc* **117**, 201–210.

Marschallinger, R. (1998). Three-dimensional reconstruction and modeling of microstructures and microchemistry in geological materials. *Scanning* **20**, 65–73.

Midgley, P.A. & Weyland, M. (2003). 3D electron microscopy in the physical sciences: The development of Z-contrast and EFTEM tomography. *Ultramicroscopy* **96**, 413–431.

Miller, M.K. (1997). Three-dimensional atom probes. *J Microsc* **186**, 1–16.

Möbus, G., Doole, R.C. & Inkson, B.J. (2003). Spectroscopic electron tomography. *Ultramicroscopy* **96**, 433–451.

Möbus, G. & Inkson, B.J. (2001). Three-dimensional reconstruction of buried nanoparticles by element sensitive tomography based upon inelastically scattered electrons. *Appl Phys Lett* **79**, 1369–1371.

Ohlhausen, J.A., Keenan, M.R., Kotula, P.G. & Peebles, D.E. (2004). Multivariate statistical analysis of time-of-flight secondary ion mass spectrometry images using AXSIA. *Appl Surf Sci* **231–232**, 230–234.

Patkin, A.J. & Morrison, G.H. (1982). Secondary ion mass spectrometric image depth profiling for three-dimensional elemental analysis. *Anal Chem* **54**, 2–5.

Rüdenauer, F.G. (1982). Instrumental aspects of spatially 3-dimensional SIMS analysis. In *Secondary Ion Mass Spectrometry: SIMS3*, Benninghoven, A., Gilber, J., László, J., Riedel, M. & Werner, H.W. (Eds.), pp. 2–21. Berlin: Springer.

Rüdenauer, F.G. (1993). Spatially multidimensional secondary ion mass spectrometry analysis. *Analytica Chimica Acta* **297**, 197–230.

Saadi, A., Lempereur, I., Sharonov, S., Autran, J.C. & Manfait, M. (1998). Spatial distribution of phenolic materials in durum wheat grain as probed by confocal fluorescence spectral imaging. *J Cereal Sci* **28**, 107–114.

Sakamoto, T., Cheng, Z., Takahashi, M., Owari, M. & Nihei, Y. (1998). Development of an ion and electron dual focused beam apparatus for three-dimensional microanalysis. *Jpn J Appl Phys* **37**, 2051–2056.

Schofield, R.M.S. (1995). Applications of ion-beam tomographic element microanalysis. *Nucl Instrum Methods Phys Res B* **104**, 212–221.

Schofield, R.M.S. & Lefevre, H.W. (1992). PIXE-STIM microtomography: Zinc and manganese concentrations in a scorpion stinger. *Nucl Instrum Methods Phys Res B* **72**, 104–110.

Sharonov, S., Nabiev, I., Chourpa, I., Feofanov, A., Valisa, P. & Manfait, M. (1994). Confocal three-dimensional scanning laser Raman-SERS-Fluorescence microprobe: Spectral imaging and high-resolution applications. *J Raman Spectrosc* **25**, 699–707.

Smentkowski, V.S, Ohlhausen, J.A., Kotula, P.G. & Keenan, M.R. (2004). Multivariate statistical analysis of time-of-flight secondary ion mass spectrometry images—Looking beyond the obvious. *Appl Surf Sci* **231–232**, 230–234.

Takanashi, K., Wu, H., Ono, N., Cheng, Zh.H., Sakamoto, T., Owari, M. & Nihei, Y. (2000). Three-dimensional microanalysis of the wire-pad contact region of integrated circuit. *Instrum Phys Conf Ser* **165**, 355–356.

Tauler, R. & de Juan, A. (2002). Multivariate curve resolution home page. http://www.ub.es/gesq/mcr/mcr.htm, last updated October 2004.

Vekemans, B., Vincze, L., Brenker, F.E. & Adams, F. (2004). Processing of three-dimensional microscopic X-ray fluorescence data. *J Anal Atom Spectrom* **19**, 1302–1308.